

Submitted to IEEE Transactions on Geoscience and Remote Sensing,
Dec., 6, 1999

Theoretical Description of a Bistatic System for Ocean Altimetry Using the GPS Signal

George A. Hajj, Cinzia Zuffada, and J. B. Thomas
Jet Propulsion Laboratory
California Institute of Technology
Pasadena, CA 91109

Abstract

The paper presents the fundamental characteristics of bistatic altimetry performed using the Global Positioning System (GPS) signal scattered off the ocean surface and collected by a receiver in space. The advantages of the dense and rapid surface coverage afforded by the existing GPS constellation could enable new oceanographic applications such as eddy monitoring and tracking of fast barotropic waves. To exploit the wealth of potentially available measurements, the choice of pointing direction for the receiving antenna is discussed together with the implications in terms of instrument footprint and coherence time. The theoretical reflected signal is then derived by extension of the cross-correlation process used for direct GPS signals and the characteristics of the leading edge are emphasized, to identify analogies and differences with the traditional altimetry waveform. In particular, the behavior of the derivative of the leading edge suggests a useful algorithm for extracting the mean sea height, wind speed and significant wave height. An overall range accuracy rms value is predicted for several antenna gains, pointing directions and different geometric scenarios. When averaging many measurements, the range error is progressively reduced yielding predicted accuracies in sea height with associated spatial and temporal resolutions. The effect of wind speed and significant wave height on the received signal are discussed by performing simulations with a realistic range of these variables. The range accuracy versus receiving antenna gain and scattering direction is discussed and a specific guideline on the gain necessary for altimetry from space is provided. Finally, considerations on the possibility to track phase at small elevation angles and the resulting improvement in the measurement accuracy are presented.

1. Introduction

The Global Positioning System (GPS), which was first conceived and built for the purpose of navigation, has been utilized in the last decade to study the Earth's interior, surface and environment in ways that far exceed anyone's original imagination. Scientific applications of the GPS include measuring seismic tectonic motions, Earth orientation and polar motion, gravimetry, neutral atmospheric temperature and water vapor profiling, and ionospheric electron density profiling and global monitoring. All of these applications have been well proven and provide new ways to enhance our knowledge about the Earth and its environment. More recent and less developed applications explore the possibility to utilize the GPS signals scattered off the ocean and sensed by an air- or space-borne receiver in a bistatic radar geometry, as a means of doing altimetry and scatterometry. When considering the constellation of 24 GPS transmitters and one such receiver a multistatic system is obtained, capable of intercepting bounces from several areas of the ocean simultaneously. As in traditional altimetry, the bistatic GPS reflected signal can be analyzed to derive three important descriptors of the ocean surface; the bistatic path delay from which the ocean height can be derived, the ocean surface wind and the ocean significant wave height.

Traditional altimetry, such as on Topex/Poseidon, is limited to looking in the (nominal) nadir direction and obtaining one height observation at a time below the altimeter; by contrast, a GPS receiver in low-Earth orbit (LEO) with an antenna pointed toward the Earth's surface can, in principle, track about 10 GPS reflections simultaneously, therefore providing a coverage that is an order of magnitude denser than nadir-viewing altimeters. Such dense coverage can be translated into a higher temporal and spatial resolution, therefore indicating the ability to recover certain ocean topography features or processes that are precluded with traditional altimeters. These include the possible measurements of eddies (Wu *et al.*, 1997) which play an important role in the transport of momentum, heat, salt, nutrients, and other chemical properties of the ocean. Another possible application of very rapid coverage of the ocean is the monitoring of fast moving barotropic waves that propagate across ocean basins too quickly to be seen by the Topex/Poseidon 10-day repeat cycle.

A concept for GPS-based altimetry was first proposed by Martin-Neira, (1993) and contains a high-level overall system description; additional related theoretical work modeling the expected signal waveform and accuracy is contained in Picardi *et al.*, (1998). Recently, an air-borne delay-mapping GPS receiver was developed (Garrison and Katzberg, 1997) and used in several experiments which demonstrated the capability of retrieving wind speed (Komjathy *et al.*, 1998). A theoretical model of the received GPS signal scattered off the ocean surface and its relationship to wind speed is detailed in (Zavorotny and Voronovich, 1999).

None of these papers discuss in detail several very important issues with regard to space-based ocean altimetry, such as coverage, resolution, accuracy and feasibility. The aim of this paper is to address these issues in some depth. In connection to this we discuss the scattered signal waveform and suggest a novel approach of deriving ocean height, surface wind and significant wave heights. This paper focuses on GPS altimetry from space-borne receivers, although many of the principles discussed here are applicable to air-borne receivers as well. This paper is organized as follow. Section 2 discusses the altimetry coverage from a receiver in LEO as a function of the receiving antenna field-of-view and pointing. Section 3 discusses the bistatic altimetry footprint and the associated coherence time and their dependence on several factors which include: (1) the elevation of the scattered signal, (2) the direction of the incidence plane relative to the LEO satellite's velocity and (3) the receiver's integration time. Section 4 describes the scattered waveform and suggests a specific approach to derive mean sea height, surface wind and significant wave height. In that section, we investigate in some detail the effect of wind, ocean roughness, and Electro-Magnetic (EM) bias on the scattered waveform. In section 5 we examine the expected range accuracy for GPS-space-borne altimetry as a function of the receiver's viewing angle and antenna gain. In section 6 we examine the likelihood of phase tracking. A discussion and a conclusion are given in section 7.

When discussing the various issues (e.g., coverage, footprint, scattered signal waveform, etc.) certain approximations of the surface will be made as needed. The assumptions used for the surface will be explicitly stated when needed.

2. Coverage

When discussing the coverage of GPS altimetry, it is sufficient to treat the ocean surface as a perfect sphere with a well defined "specular reflection" point. Fig. 1 shows a representative daily coverage of one receiver in LEO tracking all visible GPS reflections down to 15° elevation (elevation here is defined with respect to the local tangent plane at the specular reflection point— ϵ in Fig. 2). Unlike Topex/Poseidon, the coverage is not regular and does not have a repeat cycle; however, it is an order of magnitude denser

provided that the receiving antenna has a sufficiently large field of view. Because the advantage of GPS altimetry lies mostly in its potentially very dense and rapid coverage, it is important to quantify the coverage in more detail and understand the issues involved there.

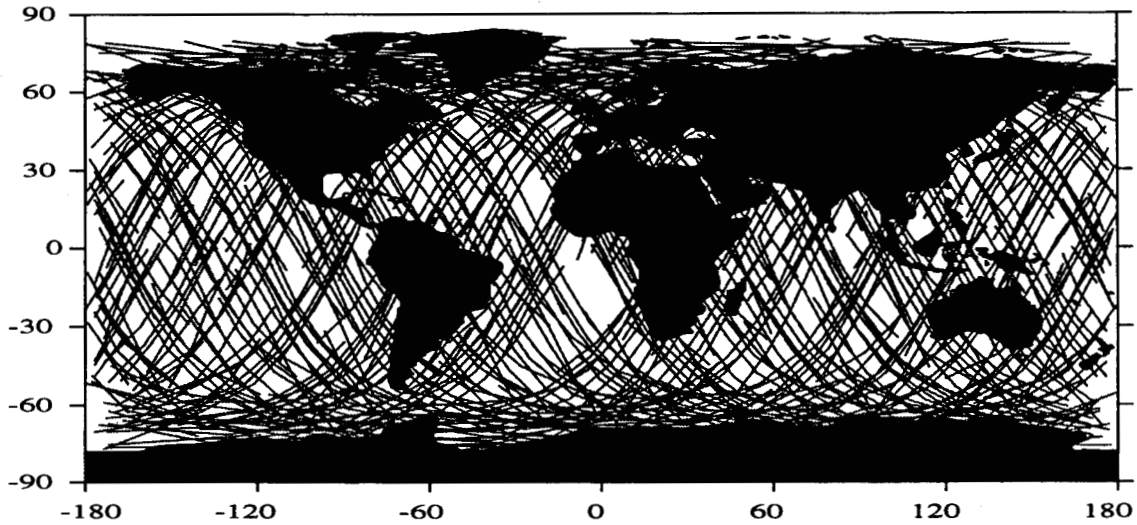


Figure 1: A representative daily coverage of ocean altimetry with GPS and one LEO satellite

Consider the geometry of Fig. 2 where the GPS signal is reflected off the ocean surface at the specular reflection point and received by a satellite in LEO. We define the following variables:

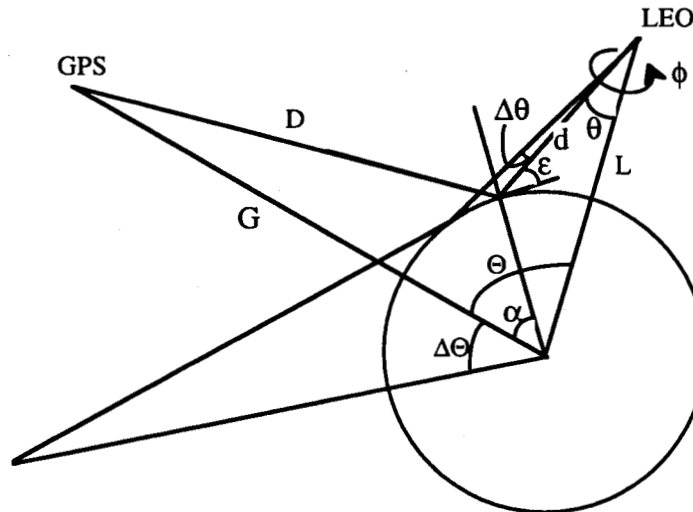


Figure 2: A pictorial representation of the bistatic ocean reflection geometry between GPS and a LEO satellite.

- θ is the receiver's viewing angle (angle between scattered signal and the LEO satellite nadir)
- ϕ is the angle out of the plane in the azimuthal direction of the receiving antenna
- ϵ is the elevation of scattered signal with respect to local tangent plane
- d and D are the distances from the specular reflection point to the LEO and GPS satellites, respectively
- L and G the LEO and GPS satellites' radii, respectively

α is the angle between the specular reflection point and the GPS satellite as seen from the Earth's center
 Θ is the angle between the GPS and the LEO satellite as seen from the Earth's center
 R is the Earth's radius
 $\Delta\Theta$ is an increment in Θ corresponding to an increment $\Delta\theta$ in θ

These variables are related through the following relations:

$$d^2 + L^2 - 2dL \cos \theta = R^2 \Rightarrow d = L \cos \theta - \sqrt{R^2 - L^2 \sin^2 \theta} \quad (1.a)$$

$$d^2 + R^2 + 2dR \sin \varepsilon = L^2 \quad (1.b)$$

$$D^2 + R^2 + 2DR \sin \varepsilon = G^2 \Rightarrow D = -R \sin \varepsilon + \sqrt{G^2 - R^2 \cos^2 \varepsilon} \quad (1.c)$$

$$R^2 + G^2 - 2RG \cos \alpha = D^2 \quad (1.d)$$

$$\Theta = \frac{\pi}{2} + \alpha - \theta - \varepsilon \quad (1.e)$$

Given L , G and θ , we can derive d , ε , D , α and Θ from 1.a-1.e, respectively.

Given the GPS satellites altitude of 20,000 km, and a receiver at 700 km altitude, we obtain the dependence of ε and Θ on the viewing angle θ as shown in figure 3.a. Note that for values of $\theta < 40^\circ$, Θ grows linearly with θ . Beyond $\theta = 40^\circ$, Θ grows faster than linear, and increases particularly fast at $\theta > 60^\circ$. This has very important implications on the visible number of reflected GPS signals. To quantify this, consider the solid angle covered by an antenna with the two angular limits of its half power beamwidth (HPBW) in the directions of θ and $\theta + \Delta\theta$, with a full azimuthal view. The corresponding reflection angles are Θ and $\Theta + \Delta\Theta$ as shown in Figure 2. The solid angle covered by such an antenna, Ω , and the corresponding average number of simultaneously visible GPS satellites are given by

$$\Omega = \int_{\phi=0}^{2\pi} \int_{\Theta}^{\Theta+\Delta\Theta} \sin \Theta d\Theta d\phi = 2\pi(\cos \Theta - \cos(\Theta + \Delta\Theta)) \quad (2.a)$$

$$N_{GPS} = 24 \frac{\Omega}{4\pi} \quad (2.b)$$

In deriving Eq. (2.b), we assumed that there are 24 transmitting GPS satellites distributed uniformly in their sphere. (Currently the GPS constellation consists of 24 satellites and 3 spares)

Figure 3.b shows the number of simultaneously visible GPS reflections by a receiver at 700 km altitude per degree of θ and cumulative from 0 to θ . From this figure we see, for instance, that the average number of simultaneously visible GPS satellites between $\theta = 0^\circ$ and 55° (HPBW = 110°) is 6.5, while this number is 7 for θ between 55° and 64.2° (HPBW = 9.2°). Table 1 lists three examples corresponding to (1) an antenna pointing toward nadir with HPBW of 90° (2) an antenna pointing toward nadir with HPBW of 120° needed to see a minimum of 8 GPS satellites, and (3) a doughnut shaped antenna beam pointing close to the limb.

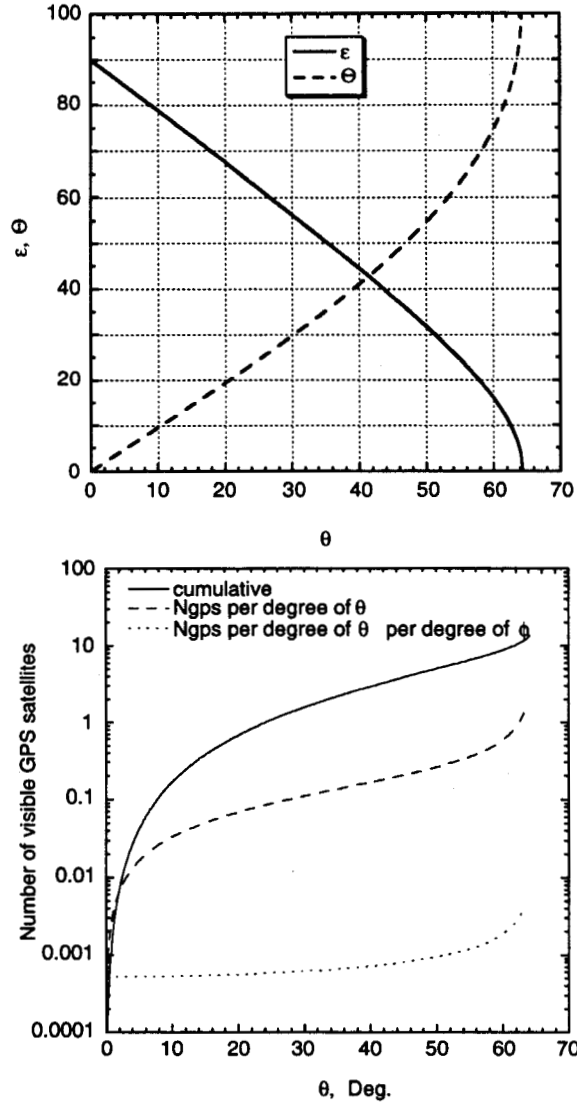


Figure 3: (a-top) ϵ and Θ as a function of θ . All angles are defined in figure 2. (b-bottom) Average number of simultaneously visible GPS satellites for three different solid angles; (1) per degree of θ and per degree of ϕ (dotted curve); (2) per degree of θ and full azimuthal view (dashed); (3) for a solid angle between $0-\theta$ deg. and full azimuthal view. The dotted curve corresponds to the dashed curve multiplied by the factor $1/(360 \sin \theta)$.

Table 1: Examples of different antenna field-of-views and the corresponding average number of simultaneously visible GPS satellites. The maximum usable θ for a receiver at 700 km altitude is $\sim 64.3^\circ$ which corresponds to the Earth's limb ($\epsilon = 0$).

Example 1: A 90° HPBW pointing toward nadir	Example 2: A 120° HPBW pointing toward nadir	Example 3: Doughnut shaped antenna beam pointing close to the Earth's limb
$\theta = 0^\circ$ $\theta + \Delta\theta = 45^\circ$ (corresponding $\epsilon = 45^\circ$) $\Theta = 0^\circ$ $\Theta + \Delta\Theta = 47.4^\circ$ $N_{\text{GPS}} = 3.9$	$\theta = 0^\circ$ $\theta + \Delta\theta = 60^\circ$ (corresponding $\epsilon = 15^\circ$) $\Theta = 0^\circ$ $\Theta + \Delta\Theta = 74.5^\circ$ $N_{\text{GPS}} = 8.8$	$\theta = 50^\circ$ $\theta + \Delta\theta = 64.2^\circ$ (corresponding $\epsilon = 2.2^\circ$) $\Theta = 54.5^\circ$ $\Theta + \Delta\Theta = 97.3^\circ$ $N_{\text{GPS}} = 8.5$

In addition to gaining more visibility as we point the receiving antenna away from nadir, the signal-to-noise ratio becomes higher and the measured scattered signal delay becomes more accurate as discussed in section 5. However, there are several disadvantages associated with pointing too far from nadir (i.e., too close to the limb) which include: (1) the surface scattering cross section starts to decrease at low elevations, (2) the sensitivity to ocean height is weaker at lower elevations, (3) the scattering footprint gets larger at lower elevation. All these factors would have to be carefully weighted when deciding on an optimal orientation of the receiving antenna.

It is important to point out that, from an engineering point of view, designing a nadir viewing antenna with 90° HPBW (such as the first example of table 1) or an off-nadir pointing antenna with 15° HPBW (such as the third example of table 3), both covering 360° in azimuth, may be equally demanding. This is because the solid angles defined by the HPBW for both antennas are nearly equal (note that this is not the same solid angle defined in 2.b). Deciding which antenna is easier to build for a given experiment will depend on several factors including the surface area available on the LEO satellite.

3. Footprint shape, size and associated coherence time

There are several factors that determine the shape of the GPS bistatic altimetry footprint. These factors include the elevation of the scattered signal, the relative direction of the incidence plane (defined according to specular reflection geometry) and the LEO satellite velocity, and the range and Doppler filter implemented in the receiver. This section examines these factors by first providing an overall review and later considering some limiting cases.

3.1 Footprint shape

In determining the shape of the scattering area relevant for altimetry (referred to as footprint) we can ignore the surface roughness since its scale is small relative to the size of the footprint. This assumption is valid as long as the ocean roughness is sufficiently large where signals coming from different points of the ocean can be considered to be incoherent. In the limit when the surface becomes very smooth relative to GPS wavelengths (expectedly a rare situation), the surface acts as a mirror where we get a coherent reflection. This limit is discussed separately in section 6.

While an exact determination of the footprint shape requires knowledge of the mean sea surface, a first-order approximation, which is used in this section, is to model the ocean surface as a plane tangent to a spherical Earth at the specular reflection point. This turns out to be an extremely good approximation (as we shall see below) because the altimetry footprint is very small relative to the curvature of the Earth.

Each GPS satellite transmits two carrier frequencies at L-band ($L1 = 1.6$ GHz, and $L2 = 1.2$ GHz) modulated by a pseudo-random code (P-code), at the rate of 10.23 MHz (~ 30 m wavelength, duration of ~ 0.1 μ sec, referred to as "chip"). In addition, the $L1$ carrier has a quadrature signal that is modulated by a Coarse Acquisition code (C/A-code) at one-tenth the P-code rate. When tracking the direct signal, a GPS receiver measures the carrier phase, essentially by a phase-locked loop, and the pseudorange¹ by searching for the

¹ Pseudorange is the speed of light times the delay between the transmitter's clock and the receiver's clock. It includes the transmitter's and receiver's clock drifts, the geometrical range, and the atmospheric and ionospheric delay.

maximum correlation between the received P-code or C/A-code and an internally generated delayed model of the code.

When the GPS signal is scattered off the ocean surface, the smallest expected delay, L_s , corresponds to that of the specular reflection point determined based on the mean sea surface. The footprint associated with delays between L_s and $L_s + \Lambda/2$ is an ellipse with semi-major and -minor axes given by

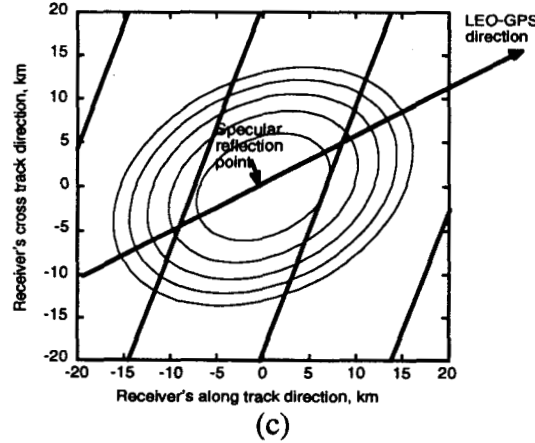
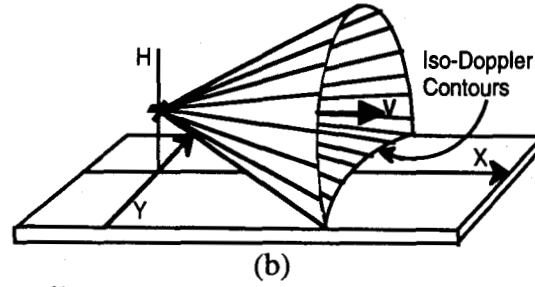
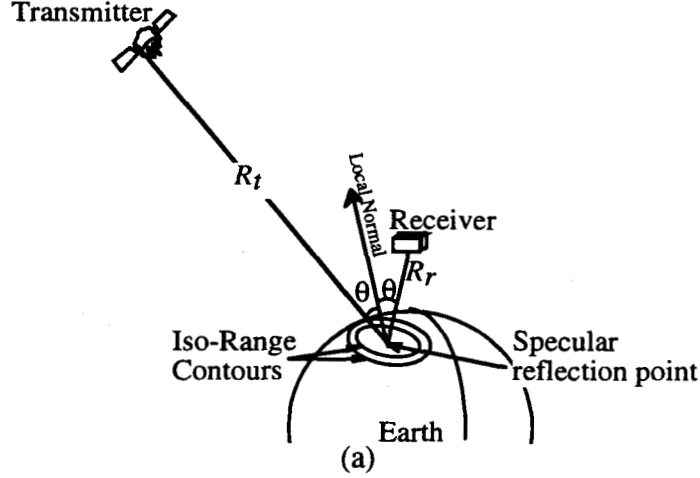


Figure 4: (a) Depiction of the bistatic reflection geometry of GPS signal off the Earth surface and the first two iso-range contours. (b) Iso-Doppler contour is defined (ignoring the GPS satellite motion) by the intersection of the ocean surface and a cone with its focal point at the receiver and its axis in the direction of receiver's velocity. (c) Intersection of iso-Doppler (appearing as nearly straight parallel lines) and iso-range (ellipses) contours on ocean surface defining footprints of bistatic reflection measurements.

$$a = \frac{\Delta x}{2} = \frac{1}{\sin \epsilon} \left(\frac{dD\Lambda}{d+D} \right)^{1/2}, \quad b = \frac{\Delta y}{2} = \left(\frac{dD\Lambda}{d+D} \right)^{1/2} \quad (3)$$

to first order in Λ/d and Λ/D . The variables of Eq. (3) are defined in figure 2. This ellipse is defined by the intersection of a spheroid with foci at the transmitter and receiver with the tangent plane at the specular reflection point (See figures 4.a and 4.c). In Eq. (3), a remains accurate to better than 2% above 10° elevation and to better than 10% above 1.6° elevation, while b is practically unaffected by the curvature of the Earth.

When tracking a GPS reflected signal, phase coherence is expected to be lost in a few milliseconds due to ocean roughness. This, in addition to the generally small reflected signal-to-noise ratio (SNR), make it impossible to lock on to the phase, except when the scattering surface is sufficiently smooth (as discussed in section 6). However, measurement of pseudorange is possible by coherently correlating the received signal and a delayed version of the modulating code over a few milliseconds during which the received signal is coherent and then incoherently averaging the amplitude of thousands of correlation functions obtained over a few seconds (Lowe et al., 1999).

The n -th annulus of Fig. 4.c is the area between the two ellipses corresponding to delays $L_s + (n-1)\Lambda/2$ and $L_s + n\Lambda/2$, where $\Lambda = 1$ P-code chip.

In addition to the time delay, the scattered signal is also Doppler-shifted by an amount determined mainly by the angle between the direction of the scattered signal and the velocity of the receiver as depicted in figure 4.b. To first order the iso-Doppler lines are hyperbolas with a symmetry axis defined by the projection of the receiver's velocity on the Earth's surface (contribution due to the transmitter can be neglected). Figure 4.c shows the iso-Doppler contours (appearing as nearly straight parallel lines) on the Earth surface, corresponding to a receiver at 700 km altitude, 45° incident angle, and a Doppler-shift separation of 250 Hz between adjacent lines. While the smallest footprint, set by the first ellipse of figure 4.c, is of order $(10 \text{ km})^2$ for a spaceborne receiver and 1 km^2 for an airborne receiver, the actual resolution is set by the size of Λ and the non-coherent averaging time necessary to reach a certain accuracy, as discussed later.

While figure 4.c depicts the general shape of a footprint defined by the intersection of iso-range and iso-Doppler lines, for our discussion we consider two limiting cases:

Case one: LEO satellite's velocity is parallel to the incidence plane

This case can be represented by the geometry of figure 2 by imagining the LEO satellite to be moving in the same plane as the reflected ray (we will refer to this plane as the *incidence plane*, the plane perpendicular to that will be referred to as the *normal plane*). In this geometry the footprint of the reflected signal is given by the intersection of the iso-Doppler lines and the iso-range lines as depicted in figure 5.a. Two points on the surface separated by distance Δx will have a Doppler shift separation of B given by

$$B = \frac{\Delta x}{\lambda} \sin \epsilon \left(\frac{v_{\text{LEO}} \cos \theta}{d} - \frac{v_{\text{GPS}} \cos \theta_{\text{GPS}}}{D} \right) \quad (4)$$

where λ is the carrier wavelength, v_{LEO} and v_{GPS} are the velocity components of the satellites in the incidence plane, θ_{GPS} is the angle from the GPS satellite nadir to the reflection point

($\theta_{\text{GPS}} < 14^\circ$). (We note that for a receiver in space the contribution due to the GPS motion is no more than $\sim 5\%$ of the total Doppler shift and will be ignored.) Therefore, a receiver with a bandwidth B will set the resolution in the LEO velocity direction to be equal to Δx .

Case two: LEO satellite's velocity is perpendicular to the plane of incidence

This case can be represented by the geometry of figure 2 by imagining the LEO satellite to be moving out of the page. In this geometry, the elongated part of the ellipse is parallel to the iso-Doppler lines (see figure 5.b); the filter bandwidth and the distance between iso-Doppler lines are related by (ignoring the GPS motion)

$$B = \frac{v_{\text{LEO}}}{\lambda} \frac{\Delta y}{d} \quad (5)$$

We note that there is no dependence on elevation, ϵ , in Eq. (5).

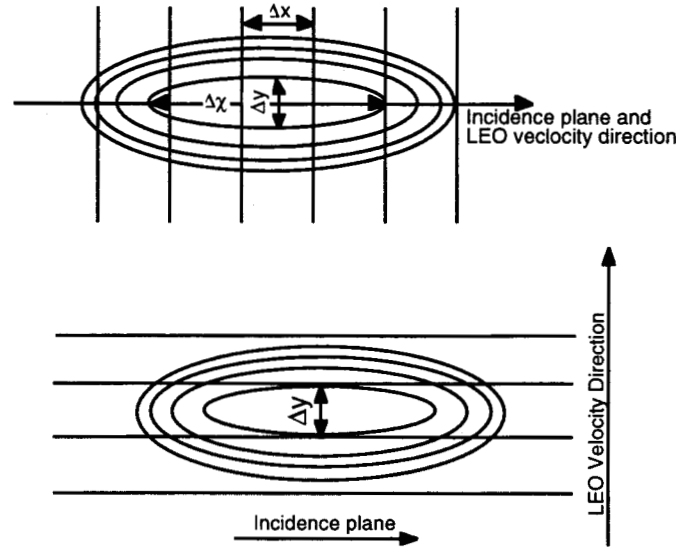


Figure 5: Division of ocean surface by iso-range (ellipses) and iso-Doppler (straight lines) when the LEO satellite's velocity is in the incidence plane (a-top) and in the normal plane (b-bottom).

3.2 Footprint size

The footprint shape and size depend on several factors: (1) The specific iso-range that is considered to be necessary for signal detection (e.g., the iso-range of figure 4.c corresponds to $1/2$ P-code chip); (2) The Doppler filter in the receiver which determines the boundaries between iso-Doppler lines; (3) The direction of the incidence plane relative to the LEO satellite's velocity; (4) The LEO antenna viewing angle; and (5) the LEO antenna field-of-view in the event when it is very narrow. In what follows we quantify these effects in some detail for the two different cases discussed in section 3.1 and depicted in figures 5.a and 5.b.

Case one: $V_{\text{LEO}} \parallel$ to incidence plane

In this case the resolution in the direction of the incidence plane is set by the smallest of Δx given by Eq. (4) and $\Delta \chi$ (indicated in figure 5.a and given by twice a in Eq. (3)). Δx and $\Delta \chi$ depend on our choices of the Doppler filter bandwidth B and the delay Λ , respectively.

We distinguish between two possible choices which we refer to below as iso-range-limit and iso-Doppler-limit.

In the “iso-range-limit” the footprint size in the incidence plane is set by the major axis of the smallest ellipse of figure 5.a. In this case the optimal choice of the Doppler filter bandwidth is given by Eq. (4) with $\Delta x = \Delta \chi$. A choice of B which corresponds to $\Delta x > \Delta \chi$ is not optimal since it does not improve the resolution while it increases the receiver's noise. In the “iso-Doppler-limit” the Doppler filter bandwidth is chosen such that $\Delta x < \Delta \chi$ in order not to exceed a desired footprint size.

In order to illustrate these two choices, consider the example of figure 6 which shows the size of the footprint as a function of the viewing angle. In the non-flat portion of the curve, the dimension of the footprint in the incidence plane is set by a of Eq. (3) with $\Lambda = 1$ P-code. When $\Delta \chi$ exceeds, for example, 50 km, then the “iso-Doppler-limit” can be applied to maintain the size of the footprint in the incidence plane to 50 km (the flat portion of the curve). The dashed portion of the curve corresponds to the size of the footprint if we were to continue to expand the Doppler limit to match the size of the first iso-range ellipse.

The size of the footprint in the normal plane is independent of the choice of the Doppler filter bandwidth and is given by twice b in Eq. (3). The dependence of b on the viewing angle is shown by the dotted curve of figure 6 for $\Lambda = 1$ P-code.

Case two: $V_{LEO} \perp$ to incidence plane

In this case (figure 5.b) the elongated part of the ellipse is parallel rather than perpendicular to the iso-Doppler lines, therefore the resolution in the incidence plane cannot be improved by applying the Doppler filter limit as in the first case. The resolution in the incidence and normal planes are given by the dashed curve (which overlaps with the non-flat part of the solid curve) and dotted curve of figure 6, respectively.

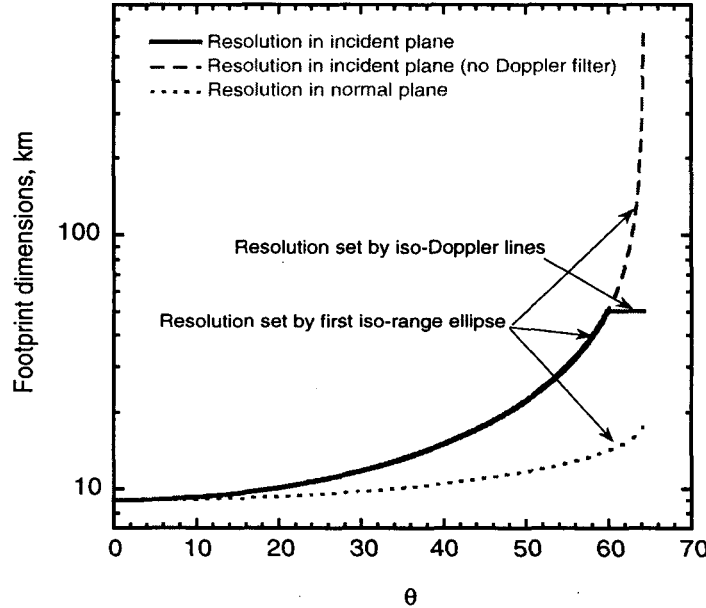


Figure 6: Solid curve: incidence plane resolution using the “iso-Doppler limit” explained above. Dashed curve: incidence plane resolution defined by the dimension of the smallest ellipse (the dashed and solid curves overlap for $\theta < 60^\circ$). Dotted curve: resolution in the normal plane.

There are several implications to the growing footprint for larger viewing angles (smaller elevations). First, the resolution is worse. Second, the radiating surface is larger, therefore increasing the signal strength. Third, the coherence time of the scattered signal is larger, further enhancing the detectability of the signal as discussed below.

3.3 Coherence time

When the ocean is rough relative to the GPS carrier wavelengths, the entire ocean can be thought of as a radiating object. In this case it is helpful to describe the ocean as a large ensemble of scattering cells, and the scattered signal can be modeled as the superposition of the returns from each element, each with different time delay τ_k , phase ϕ_k , and amplitude α_k , therefore we write received electric field as

$$E_{LEO} = \sum_k \alpha_k e^{-i\left(\frac{2\pi c}{\lambda} \tau_k + \phi_k\right)} \quad (6)$$

where c is the speed of light and λ is the carrier wavelength. Over a short time scale where the surface can be assumed to be stationary, the radiated pattern of the ocean will not change and the receiver will travel across several wave fronts. Here we would like to determine the coherence time, t_{coh} , which is defined as the time it takes the receiver to travel across two wavefronts.

Given a radiating surface area defined by the footprint as discussed in section 3.2, consider the radiation from any two points (1) and (2) inside that area (see Fig. 7). Assuming the two points are radiating toward the receiver with the same power level, an assumption that is satisfied whenever the footprint is small relative to the glistening zone², the radiated field at the receiver from these two points is proportional to

$$\cos\left(\frac{2\pi}{\lambda} d_1 + \phi_1\right) + \cos\left(\frac{2\pi}{\lambda} d_2 + \phi_2\right) = 2 \cos\left[\frac{2\pi}{\lambda} (d_1 + d_2) + \phi_1 + \phi_2\right] \cos\left[\frac{2\pi}{\lambda} (d_1 - d_2) + \phi_1 - \phi_2\right]$$

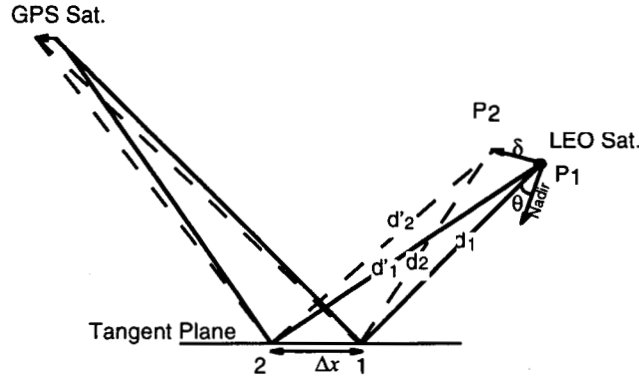


Figure 7. Pictorial representation of reflection from two points, a_1 and a_2 , on the surface of the ocean at two different times

Ignoring the GPS motion, as the receiver moves we note that (1) the term $(d_1 - d_2)$ varies more rapidly than $(d_1 + d_2)$, (2) the variation of $(d_1 - d_2)$ is most rapid when the two points are in the plane defined by the receiver's velocity vector and the direction of the reflected signal, and (3) the variation of $(d_1 - d_2)$ is most rapid when the distance between the two

² The glistening zone is defined as the area on the ocean delimited by a scattering coefficient equal to $1/e$ of the maximum, occurring at the specular reflection..

points in the aforementioned plane is maximized. Therefore, the coherence time, t_{coh} , is set by the two boundary points on the footprint in the plane defined by the receiver's velocity vector and the direction of the reflected signal. Once these two points are determined, t_{coh} is given by δ/c where δ is the distance the receiver has to travel such that $(d_1 - d_2) - (d'_1 - d'_2)$ is equal to one carrier wavelength (see Fig. 7).

Considering the two cases 1 and 2 of section 3.2 (V_{LEO} parallel and perpendicular to incidence plane, respectively), the coherence time in the first case is set by the shorter of Δx and $\Delta \chi$ on Fig. 5.a and corresponds to the inverse of B given in Eq. (4), while in case 2 it is set by Δy of Fig. 5.b and corresponds to the inverse of B given in Eq. (5). The dependence of the coherence time on the viewing angle is shown in Fig. 8. The following observations are in order:

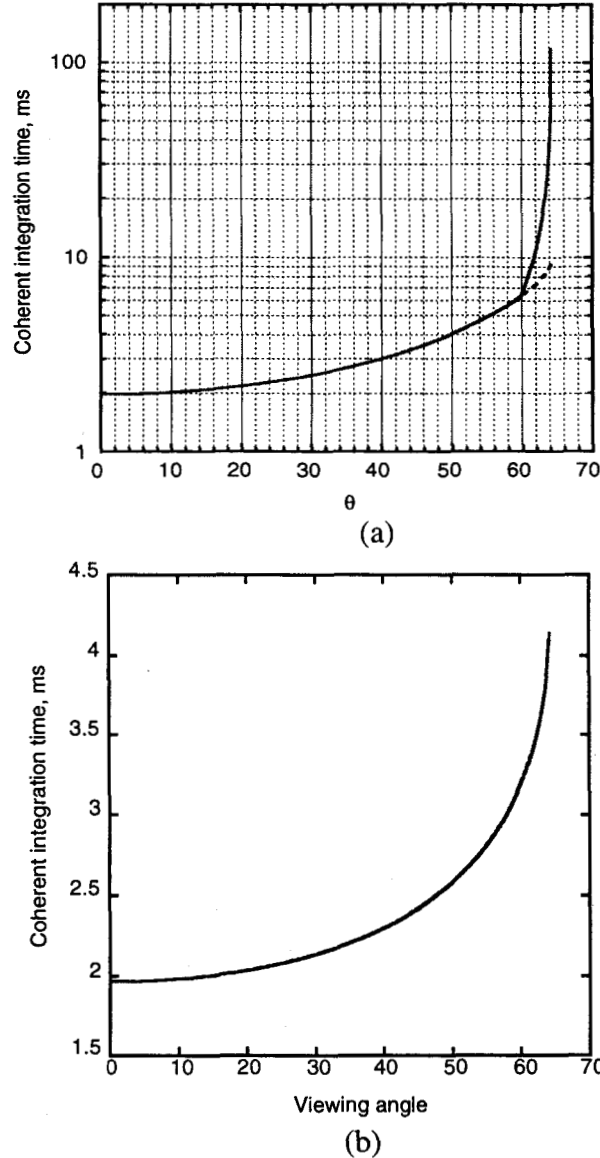


Figure 8: (a) Coherence time for case one. The solid curve corresponds to the solid curve of Fig. 6. The dashed portion corresponds to the dashed portion of Fig. 6 where the Doppler filter is set by the size of the first iso-range ellipse. (b) Coherent integration time for case two.

- (1) In both cases 1 and 2 the coherence time grows for larger viewing angle (smaller elevation)
- (2) The very rapid growth of the coherence time indicated by the solid curve of Fig. 8.a at $\theta > 60^\circ$ corresponds to the point at which the “iso-Doppler limit” is applied (the solid curve of Fig. 6 where Δx becomes $< \Delta \chi$). This rapid growth is due to a smaller ϵ , larger θ and larger d in Eq. 4 which correspond to the following physical reasons, respectively: (a) The effective radiating area on the surface as viewed by a satellite at elevation ϵ scales as $\sin(\epsilon)$, (b) the Doppler shift rate grows as $\cos(\theta)$, and (c) the angular separation between two points of fixed distance on the ocean as viewed by a LEO satellite decreases as $1/d$.
- (3) The dashed portion of the curve in Fig. 8.a corresponds to the coherent integration time if we were to continue to expand the Doppler iso-range to match the size of the first iso-range ellipse.
- (4) Coherence time estimated here is based on a rough random surface which is stationary. Realistically, ocean waves change their relative shapes over a time scale known as ocean correlation time. Once the ocean correlation time is established for L-band, the part of the curves in Fig. 8 for which the coherence time is larger than the ocean correlation time becomes invalid.
- (5) The increase of coherence time implies that we can afford to have less antenna gain when at larger viewing angles to obtain the same range accuracy. This will be discussed later on in the paper.

4. GPS altimetry and derivable physical quantities

4.1 Reflected signal “waveform”

As already stated, we are modeling the received signal as the sum of returns from a very large number of independent scatterers on the ocean surface, as given by Eq. (6). The time delay τ_k can be easily determined based on the positions of the transmitter, the receiver and the k -th scattering element on the surface. The phase ϕ_k is a complicated function of the electromagnetic properties and roughness of the scattering element and the polarization of the signal. The amplitude α_k is the square root of the scattered power, P_k , which is given by the radar equation

$$P_k = \left(\frac{P_t G_t}{4\pi D_k^2} \right) \left(\frac{\sigma_{0k} A_k}{4\pi d_k^2} \right) \left(\frac{\lambda^2 G_r}{4\pi} \right) \quad (7)$$

with:

P_t transmitted power

G_t transmitter's antenna gain

D_k, d_k distances from the transmitter and receiver to the k -th scattering element, respectively

σ_{0k} scattering cross section coefficient

A_k the k -th element scattering area

G_r receiver's antenna gain

When tracking the direct signal, a GPS receiver measures the pseudorange by searching for the maximum correlation between the received P-code and an internally generated delayed model of the same P-code. In the limit of a perfectly calm sea, the reflected signal can be thought of in the same manner as the direct signal but with a longer delay. In this case, the contribution from all terms of Eq. (6) will cancel except for one term which corresponds to specular reflection (conventionally we define it to be the first term). In this limit, when correlating the received reflected signal with a model signal of delay τ_m and phase ϕ_m , and integrating over a few milliseconds, the correlation function is approximately a triangle

function, $\Lambda(\tau_m - \tau_1)$ (Thomas, 1995) , as illustrated in Figure 9.a, multiplied by the amplitude a_1 and the phasor $\exp[i(\phi_m - \phi_1)]$.

When the surface is rough the correlation function can be modeled as

$$R_p(\tau_m) = \sum_{k=1}^{\infty} \alpha_k e^{i(\phi_m - \phi_k)} \Lambda(\tau_m - \tau_k) \quad (8)$$

Squaring Eq. (8), taking the ensemble average and explicitly writing the weighting factors from Eq. (7), we get

$$\begin{aligned} \langle R_p R_p^* \rangle(\tau_m) &= \sum_{k=1}^{\infty} \left(\frac{P_t G_t}{4\pi D_k^2} \right) \left(\frac{1}{4\pi d_k^2} \right) \left(\frac{\lambda^2 G_r}{4\pi} \right) A_k \sigma_{0k} \Lambda^2(\tau_m - \tau_k) \\ &= \left(\frac{P_t G_t}{4\pi D^2} \right) \left(\frac{1}{4\pi d^2} \right) \left(\frac{\lambda^2 G_r}{4\pi} \right) \sigma_0 \iint dxdy \Lambda^2(\tau_m - \tau(x, y)) \end{aligned} \quad (9)$$

where $dxdy$ denotes the integration over the ocean's surface. By explicitly moving all the factors multiplying Λ^2 outside the integral in Eq. (9), we are assuming that the integration is over an area that covers several iso-ranges but small relative to the glistening zone and the receiving antenna footprint; such would be the case for a receiver in space and for a sufficiently broad-beamed antennas. By assuming that the process is ergodic, we can get the equivalent of this ensemble average by incoherently averaging the few milliseconds measurements obtained over a few seconds. Figure 9.b shows a graphical representation of Eq. (9) where the solid line corresponds to the cell with the shortest possible path and the dashed lines correspond to an infinite number of cells placed around the specular point at progressively increasing distances. The sum of all these contributions gives the "ideal" correlation function shown in Fig. 9.c. This correlation function is analogous to the waveform used in traditional altimetry.

We note the following important features of this function: (1) It has a rise time of exactly 2 P-code chips, (2) the rise starts at model delay $\tau_m = \tau_1 - 1$ P-code chip, (3) It saturates at some peak (but eventually starts to drop as we move sufficiently away from the specular reflection point).

By taking the Derivative of the Correlation Function (DCF) of Figure 9.c with respect to the model time delay, we obtain the function shown in Figure 10. Note that it exhibits a sharp peak, originating from the change of concavity of the curve of Fig. 9.c, which always occurs at the lag time correspondent to the return from the shortest path. The effect of the wind speed and surface statistics introduces modifications to the ideal shape of Figure 10 in a manner that allows us to extract the important sea state parameters of interest in altimetry, as will be illustrated shortly. The following physical parameters can be derived from this function:

- (1) Mean sea height—derived from knowledge of the location of the DCF peak relative to the model delay
- (2) Ocean surface wind—derived from the height of the DCF peak
- (3) Significant wave height—derived from the width of the DCF

The derivation of these three parameters from the DCF is discussed in detail below. However, it is important to restate the assumptions under which this discussion is valid. In deriving the DCF of Fig. 10 we assumed that the surface is rough relative to the GPS wavelengths, and that the footprint corresponding to a few P-code chips is small relative to the glistening zone. The latter condition implies that the ocean is rough and that the receiver

is sufficiently high from the surface (e.g., in space). When either one of these conditions are not satisfied, the correlation function is somewhere between that of Fig. 9.a (perfectly smooth surface condition) and Fig. 9.c (rough surface condition) with a rise time and trailing edge that depend on roughness, receiver's height, and receiving antenna gain and orientation.

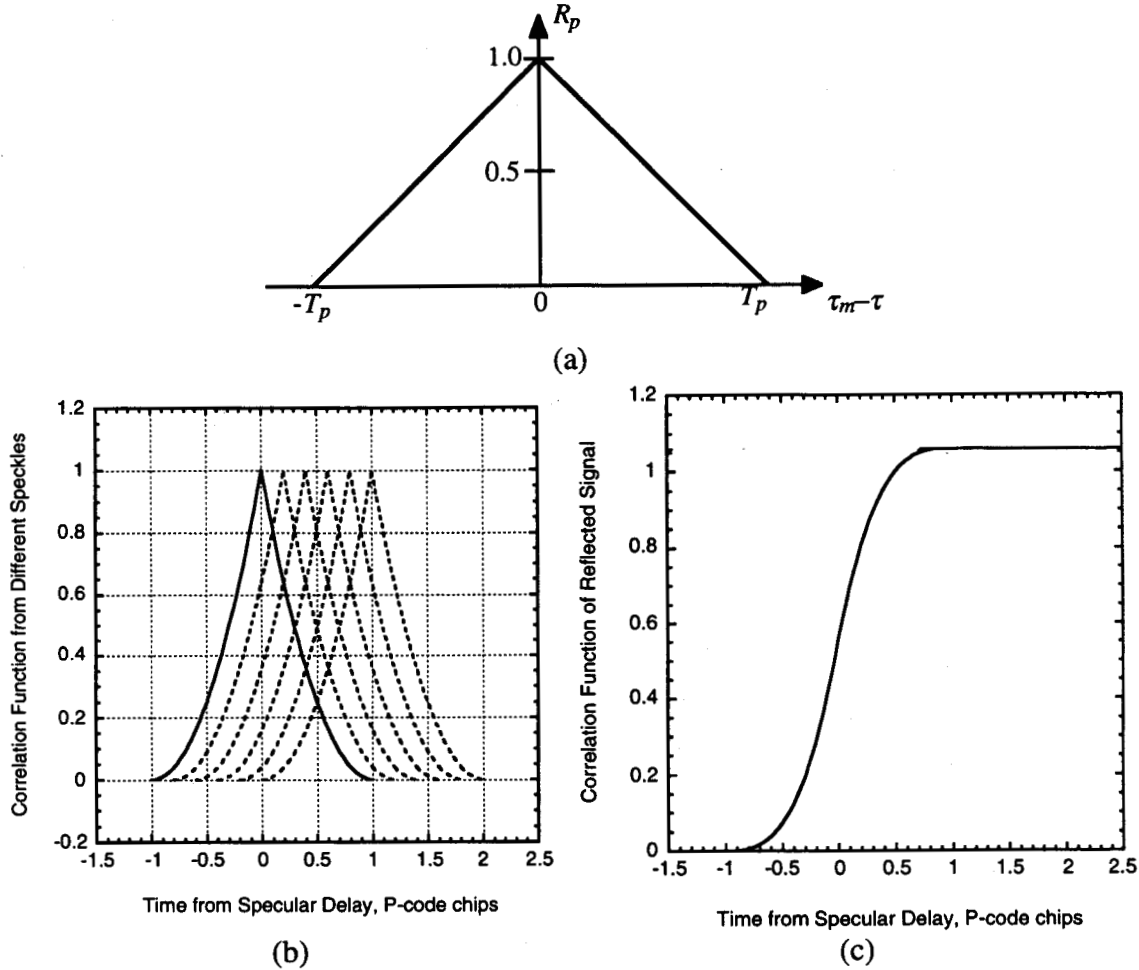


Figure 9: (a) The amplitude of the time averaged correlation function of the direct GPS signal (or reflected from a perfectly smooth surface) with delay τ , based on a model function of the P-code with a model delay τ_m . T_p is the period of one P-code chip. (b) A graphical representation of Eq. (9) where the correlation function is given as the sum of the solid line (the square figure 9.a), and the dashed lines (an infinite number of delayed replicas which correspond to reflections from favorably oriented facets around the specular point). (c) The shape of the ideal correlation function of the scattered signal.

4.2 Deriving mean sea height

The DCF of figure 10 has a sharp peak at the specular reflection point from which the path delay of the received signal can be measured. The expected accuracy of the delay measurement is discussed in detail in Section 5, here we only consider how it is possible to derive mean sea height from the bistatic path delay.

This delay measurement contains the following terms (ignoring the EM-bias for now):

- 1) Ionospheric delay

- 2) Clock drifts in the transmitter and the receiver
- 3) Neutral atmospheric delay
- 4) The path length between the GPS transmitter phase center to the specular point as defined by the mean sea surface and then to the receiver's phase center. This term is determined by the position of the transmitter and the receiver and the mean sea surface height.

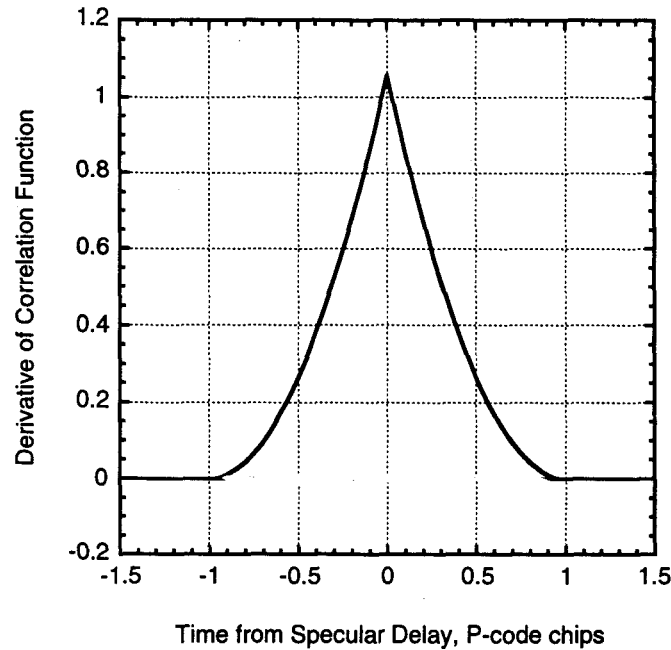


Figure 10: The derivative of the correlation function with respect to time delay in the receiver. The center of the peak is an indication of the delay of the signal from which mean sea height can be derived, the height of this function indicates the ocean roughness from which the surface wind can be derived, the width of this function indicates the ocean significant wave height.

In principle, the ionospheric delay can be solved for and removed from measurement of the dual GPS frequencies. The transmitter and receiver clocks drift can be eliminated by differencing the reflected measurement from the direct one. Neutral atmospheric delay can be calibrated to about 10 cm as discussed below. The position of the transmitter and the receiver can be determined accurately (usually to better than a decimeter) from direct measurements to the GPS satellites. Therefore, the path delay measurement can be translated into mean sea height in a similar manner to what is done for traditional altimetry.

Neutral atmospheric delay is of order $4/\sin(\epsilon)$ meters (since the signal is traveling twice through the atmosphere), 90% of which is due to the dry atmosphere. There are two methods by which the neutral atmosphere can be accounted for: (1) By solving for it, which is possible due to the different zenith-to-line-of-sight mapping functions of the neutral atmospheric delay and the delay due to uncertainty in mean sea surface height. The former goes roughly as $1/\sin(\epsilon)$ while the latter goes as $\sin(\epsilon)$. (2) By calibrating it with data obtained from a global circulation model (GCM) such as the European Center for Medium-range Weather Forecast (ECMWF) analysis. The former method has been pursued by Wu et al., (1998) and simulations indicate that, with a single receiver in LEO, assuming 75 cm range delay rms error, it is possible to obtain 15 cm ocean height accuracy over $\sim 500 \times 500 \text{ km}^2$ areas, after 1 day of averaging. Their study, however, does not account for

different temporal and spatial spectra of the ocean and the atmospheric moisture and further research is needed in this area to reach an optimal solution. In the second approach, it is possible to calibrate the atmospheric delay to better than $\sim 97\%$ (the error is mostly due to water vapor). In this case, neutral atmospheric error will be of order $\sim 15/\sin(\epsilon)$ cm. The sheer number of range measurements obtained from a receiver in LEO allows us to average down this error to a very small value, assuming there are no systematic biases in the GCM analysis. It is most likely that a hybrid between the two approaches mentioned above will provide an optimal solution, since the former approach is especially suitable for detecting any possible biases in the analysis, while the latter approach will not weaken the data strength significantly.

As discussed in section 5, the expected accuracy of range measurement for a receiver in space with a ~ 23 dB antenna is about 1 m after 4 seconds of averaging. This 1 m range random error will map to an error of $0.5/\sin(\epsilon)$ meters of ocean height, or ~ 0.7 m on average. Even though this accuracy does not reach that of traditional altimetry from space, the real advantage of doing altimetry with GPS is the dense and rapid coverage where much averaging can be done. To illustrate this point we consider the simplistic approach of averaging presented below.

Assuming that we track 8 GPS reflected signals simultaneously, a receiver in LEO will observe ~ 0.2 million 4-sec measurements of ocean height in one day. These are separated by about 25 km in the direction of the reflection point motion and an average of 100 km between tracks. By dividing the ocean into small areas, mean sea height estimates obtained from different GPS signal reflections within the same area can be averaged to reduce the random errors by the square root of the number of measurements. Table 2 summarizes the resolution and the corresponding error in height achievable from one receiver in space averaged over 1, 4 and 8 days. A small LEO constellation further improves the values due to averaging, as would the inclusion of GLONASS reflected signals. For instance, eight LEO satellites tracking GPS and GLONASS would provide global 3-cm ocean heights in 1 day over 200-km scales; or global sub-decimeter height accuracy in 4 days over 25-50 km scales, suitable for ocean mesoscale flow or eddy studies of heat transport. Needless to say, these are simplistic first-order estimates of the random errors of mean sea height which are possible with GPS altimetry; a much more elaborate study of how these errors would average down and of systematic errors must be considered before any definitive statement regarding the utility of GPS altimetry can be made.

Table 2: Resolution and corresponding accuracy obtained after 1, 4 and 8 days of averaging from a GPS receiver in LEO with about 23 dB antenna gain. Two cases are shown: single LEO with GPS, and 8-LEO constellation with GPS+GLONASS.

scale, km	Ocean height error, cm 1 LEO, GPS tracking only			Ocean height error, cm 8 LEOs, GPS+GLONASS tracking		
	1 day average	4 days average	8 days average	1 day average	4 days average	8 days average
25		76	54	38	19	13
100	38	19	13	10	5	3
200	19	10	7	5	2	2
400	10	5	3	2	1	1
1000	4	2	1	1	<1	<1

4.3 Deriving ocean surface wind

Assuming that the incident power density, the antenna gain, feed losses, and pointing geometry can all be determined, knowledge of the peak value of the DCF can be used to determine σ_0 via equation 7. In the geometric optics (GO) limit of the Kirchhoff approximation, valid at high frequencies, the dependence of σ_0 on wind speed has been postulated for some time (Brown, 1978) for the nadir geometry of traditional altimetry and, more recently, it has been extended to the bistatic geometry in (Zavorotny, 1999). Incidentally, Zavorotny discusses the dependence of wind speed on the slope of the trailing edge of the correlator output whereas we restrict our attention to the peak height of the DCF. The difficulty in Zavorotny's approach when collecting reflections from space is that the trailing edge will be nearly flat (fig. 9.c) due to the large size of the glistening zone. On the other hand, the sensitivity of the peak amplitude will increase for space-borne receivers versus air-borne ones.

According to the above referenced approaches, the ocean surface winds speed affects σ_0 through the mean square slope (mss) of the surface. If the ocean surface spectrum $\Phi(k, \varphi)$ (k is the ocean spectrum wave number, φ is the angle in azimuth) is known, the mss can be calculated from an integration of the function $k^2 \Phi(k, \varphi)$ (see, for example, Elfouhaily, 1998) over the spectral domain ranging from $k=0$ to a value k_{\max} corresponding to the smallest surface feature the operating wavelength is sensitive to. Alternatively, empirical models of mss versus wind speed have been obtained (although not at L-band) (Elfouhaily, 1998) in simple closed form (which are used to check the correctness of ocean spectra, or at least the integral of $k^2 \Phi(k, \varphi)$). Since there are several proposed ocean spectra, most of which disagree with one another in portions of the spectral range, there is ambiguity in the derivation of σ_0 versus wind speed via spectral integration, and further investigation is needed. In particular, at L-band the sensitivity of the result on the truncation point is rather high. Indeed this point raises the question of the validity of a high frequency approach such as the GO model at L-band, and more work is needed in this area. A discussion of this issue is provided by Fung et Al., 1999. Nevertheless, based on preliminary experimental validations with data taken from airplane, an accuracy in wind speed retrieval of 1-2 m/sec was observed (Komjathy, 1998), based on Zavorotny's approach.

4.4 Deriving Significant Wave Height (SWH)

Thus far, we have only considered the return from the mean sea surface and have ignored the effect of the distribution of the heights of the scattering points on the DCF. Such effect has been quantified in traditional altimetry (Brown, 1978) as introducing a convolution and we can use a similar approach here. A general probability distribution function (pdf) for scattering points is given in (Barrick and Lipa, 1985; Srokosz, 1986)

$$f_{sp}(z) = \frac{1}{\sigma\sqrt{2\pi}} \exp\left(\frac{-z^2}{2\sigma^2}\right) \left\{ 1 + \frac{z}{6\sigma} \left[\lambda_{sp} \left(\left(\frac{z}{\sigma} \right)^2 - 3 \right) - 3\gamma_{sp} \right] \right\} \quad (10)$$

where z is the surface height, σ is the height standard deviation, λ_{sp} is the ocean surface skewness, and the parameter γ_{sp} describes the deviation of the mean of the pdf from the plane $z = 0$ and thus contributes to the description of the EM bias (Rodriguez, 1988). The significant wave height is conventionally defined as $SWH = 4\sigma$. The convolution between Eqs. 9 and 10 is given by

$$C \int_{-\infty}^{+\infty} dz f(z) \int dxdy \Lambda^2(\tau_m - \tau(x, y, z)) = C \int dxdy \Lambda_R^2(\tau_m - \tau(x, y, 0)) \quad (11)$$

where

$$\Lambda_R^2 = C \int_{-\infty}^{+\infty} dz f(z) \Lambda^2\left(\tau_m - \tau(x, y, 0) + 2 \frac{z}{c} \sin(\epsilon)\right) \quad (12)$$

where ϵ is the elevation of the specular reflection ray. In obtaining Eqs. (11) and (12) we have (a) lumped all the terms outside the integral in Eq. (9) into C , (b) exchanged the integrations of dz and $dxdy$, which is valid assuming ϵ and $f(z)$ are independent of x and y over the area of integration, and (c) made use of the equality

$$\tau(x, y, z) = \tau(x, y, 0) - 2 \frac{z}{c} \sin(\epsilon) \quad (13)$$

Λ_R^2 corresponds to the square of the correlation function of a reflection from a small surface area (over which x and y are essentially constant) but accounting for the ocean roughness; it is therefore the equivalent of Λ^2 with the ocean roughness and skewness effects included.

We have performed numerical convolutions for a variety of cases, including Gaussian and skewed oceans, and illustrate the results in Fig. 11. Note that in the limiting case of a Gaussian sea with very small σ the convolution reproduces substantially the ideal correlator function Λ^2 , whereas for progressively larger σ the peak of the correlator decreases and broadens and its skirts extend beyond the original width of two chips. When skewness is included the shape of the resulting function becomes asymmetric and exhibits an offset which indicates that the time of arrival corresponding to the maximum no longer identifies the location of the mean plane, but rather the location of the mean of the surface pdf, which is lower. This error is conventionally called the EM bias (Rodriguez, 1988).

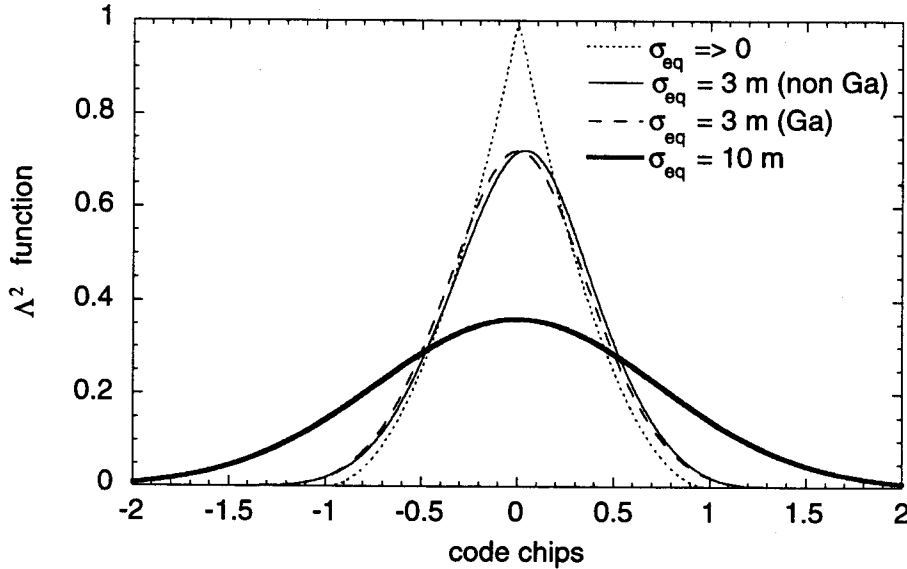


Figure 11. The Λ_R^2 function and pdf of ocean specular points. The parameter $\sigma_{eq} = \sigma \sin(\epsilon)$ has been introduced. The skewness parameters for the thin solid curve are $\lambda_{sp}=0.4$, $\gamma_{sp}=0.2$.

Now we turn our attention to the effect of the height distribution on the DCF (Fig. 10). We note that with increasing SWH the peakedness of the DCF will weaken and the peak value will decrease. An example is illustrated in Fig. 12 for the case of a very large SWH, contrasted with an ideal situation of $\text{SWH} \rightarrow 0$. Note that the location of the peak relative to the model delay shifts to lag values larger than zero; the extent of the shift is twice the EM bias. For realistic sea surfaces, this shift is of order of a few nsec, thus requiring a very high resolution to locate it (as obtained in traditional altimetry). The extent of peak smoothing and reduction is dependent on wind speed, SWH and elevation angle ϵ . In particular note that wind speed and SWH are not totally independent quantities; in fact one component of SWH is wind driven whereas another component is swell driven. In general, height, wind speed and SWH will have to be solved for simultaneously, in principle using parameter estimation techniques similar to those of retracking in traditional altimetry. At large angles of incidence the effect of SWH on the DCF is reduced since it is the component of SWH along the direction of propagation which determines the shape of the correlator and the DCF. This means that sensitivity to SWH is reduced for small values of ϵ , consistent with the fact that the ocean appears smoother and sensitivity to height is also reduced.

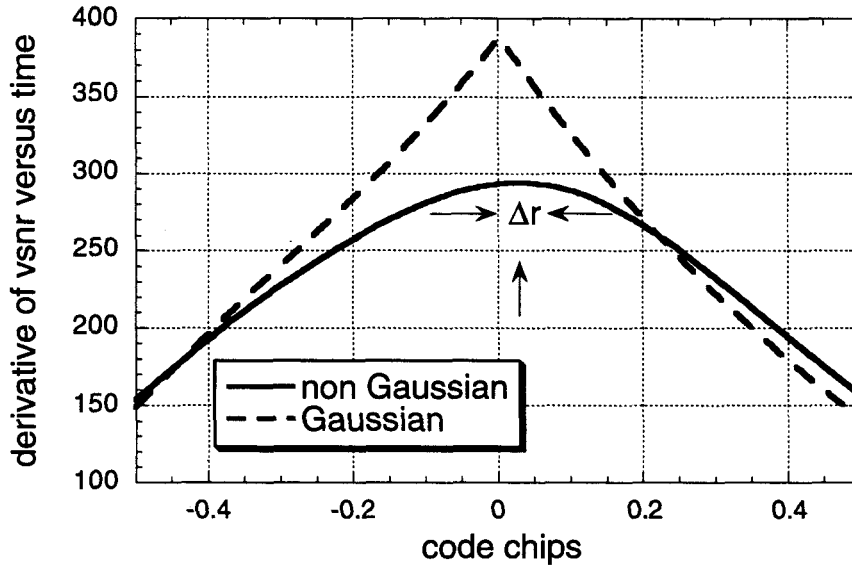


Figure 12. Effect of skewness and EM bias on the GPS altimetry DCF (Fig. 10). The same values as those of Fig. 11 were used for the non Gaussian case.

5. Accuracy of Range Measurements

We now turn our attention to estimating the range accuracy expected from a space-borne receiver. The range error (which comes from the error in determining the position of the peak of the DCF of Fig. 10) depends on several factors including (1) the sampling rate, (2) the chip-code wavelength (C/A vs. P-code), (3) the exact algorithm used in the receiver to estimate the peak location. Careful examination of these factors would require a detailed understanding of the GPS signal structure and the manner in which it is processed which would take us beyond the scope of this paper. For our purposes, we use as a proxy the relationship between range error, P-code chip wavelength and signal-to-noise ratio as given by Thomas [1995] for the direct signal, where

$$\sigma_\tau = k \frac{\lambda_{\text{code-chip}}}{VSNR} \quad (14)$$

where σ_τ is the range rms error, $\lambda_{\text{code-chip}}$ is the P-code chip wavelength, $VSNR$ is the voltage-to-noise ratio, and k is a proportionality constant which is roughly equal to 0.5. The $VSNR$ is given by the square root of Eq. (9) divided by the receiver's noise. The receiver's noise is given by $k_B TB$, where k_B is Boltzmann's constant, T is the system temperature, B is the receiver frequency bandwidth (given by Eqs. 4 and 5). Using the following assumptions:

$P_t G_t / 4\pi D^2 = -160$ dBw of received signal power levels at the ground with a 0 dBIC antenna.

$\sigma_0 = 10$ dB corresponding to average roughness. Actual roughness can vary between 0-20 dB.

A is taken to be the area of the footprint according to Fig. 6

$T = 400$ K for a receiver in space looking toward the Earth

B is given by the inverse of the solid or dashed lines of Fig. 8.

We note that the peak in Eq. (9) depends on the elevation angle via the variables d , A and B . The scattering cross section (for incoherent scattering) σ_0 is also elevation dependent and a precise bistatic characterization valid for all angles and typical sea surface roughness is still a challenging problem. Fung's general bistatic scattering model has recently been combined with a realistic ocean spectrum (Elfouhaily, 1997) to investigate roughness (wind) sensitivity versus incidence angle (Fung et Al., 1999) Based on these preliminary results we expect that the total σ_0 will be slightly increasing perhaps up to $\theta_{\text{inc}} = 70$ degs and the sensitivity to wind, expressed as differences between σ_{Vertical} and $\sigma_{\text{Horizontal}}$ is shown to increase at high angles. This is to say that the decrease in the σ_{Vertical} will be entirely compensated by an increase in the $\sigma_{\text{Horizontal}}$, the precise extent of which will depend on surface roughness. At very high incidence angles, the total σ_0 will rapidly decrease to zero, however the coherent scattering mechanism might eventually ensue, again depending on surface roughness. For the purpose of this discussion we will conservatively take σ_0 to be constant.

Using the above assumptions, we estimate the range accuracy at different viewing angles and different receiving antenna gains for the two geometrical limits considered in section 3.2. Fig. 13.a shows the range accuracy for the case when $V_{\text{LEO}} \parallel$ to incidence plane (case 1 of section 3.2) using the iso-Doppler limit to maintain a maximum footprint size of 50 km in the incidence plane. Fig. 13.b shows the range accuracy for the same geometry but using the iso-range limit and allowing the Doppler filter to expand such that the iso-Doppler lines match the iso-range footprint. The corresponding figure for the case when $V_{\text{LEO}} \perp$ to incidence plane (case 2 of section 3.2) is given in Fig. 14.

When estimating these range accuracies, the P-code is assumed to be known (no encryption). In the presence of anti-spoofing (AS), the direct P-code signal can be used to replace the modeled P-code signal; in this case, the same range accuracies can be obtained by assuming an additional 3 dB of gain for the reflection antenna and about 10 dB of antenna gain for direct signal. Figs. 13 and 14 show that there is a considerable improvement in range accuracy for scattering at smaller elevations (higher incident angles). This improvement is due to the increase in coherence time which more than compensates for the increase in the distance from the scattering surface to the LEO satellite. For instance, in all the cases considered above, for a 20 dB gain, the range accuracy will reduce

from 2 m at nadir viewing to 1 m at 60° viewing angle (corresponding to 15° elevation). This factor of 2 improvement in range is equivalent to having an additional 6 dB of gain.

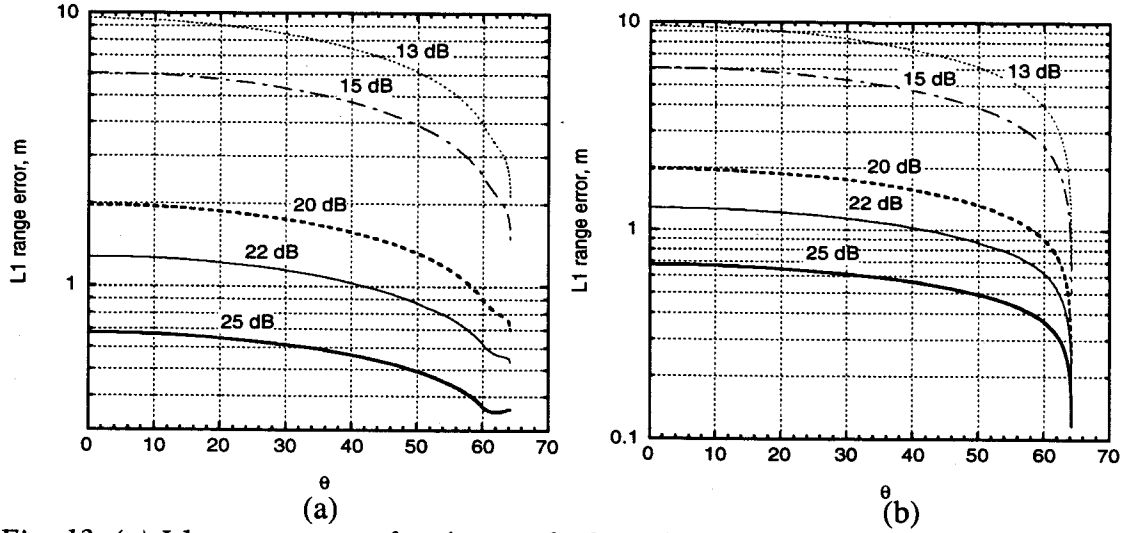


Fig. 13: (a) L1 range errors after 4 second of incoherent averaging. A Doppler filter is used to maintain a maximum footprint size of 50 km (in the incident plane). (b) Same as in (a) but for the approach where the footprint size is set by the first iso-range ellipse.

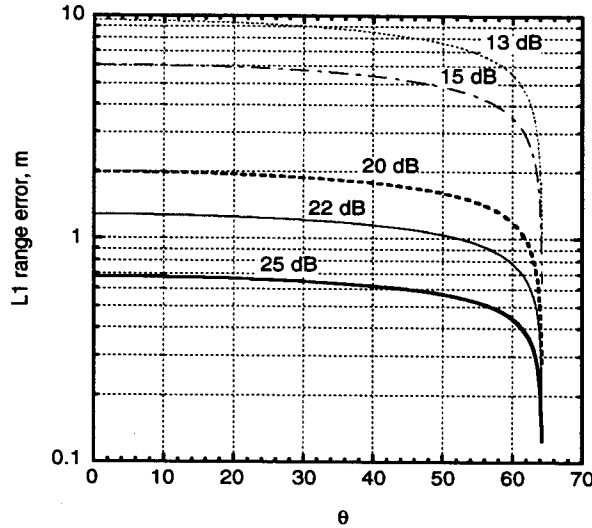


Fig 14: Range accuracy for the case when the LEO velocity is normal to the incidence plane.

6. Phase Tracking

Thus far it has been assumed that phase coherence is only maintained over a short time (1-100 ms) defined by the minimum of the temporal coherence (the time it takes for the surface to change its shape) and the spatial coherence (set by the footprint size). When the surface is smooth, this coherence time becomes irrelevant because variation in the shape of the surface will introduce a small variation in the phase making it possible to measure the phase with a phase-locked loop receiver. The Raleigh criterion is traditionally used to define the onset of incoherent scattering and is given by

$$h = \frac{\lambda}{8 \sin \epsilon} \quad (15)$$

It implies that when the wave heights exceed h , reflections from the crest and the trough are different by more than $\lambda/4$ as can be seen from simple geometrical considerations. Applying this criterion to the GPS frequencies, we plot h as a function of θ in Fig. 15. We note that the ocean scatters incoherently when $h \approx 2$ cm for normal incidence and when $h \approx 1$ m for $\theta \approx 64^\circ$ ($\epsilon \approx 2^\circ$). The former condition is nearly never satisfied while the latter condition is satisfied for a good fraction of the time.

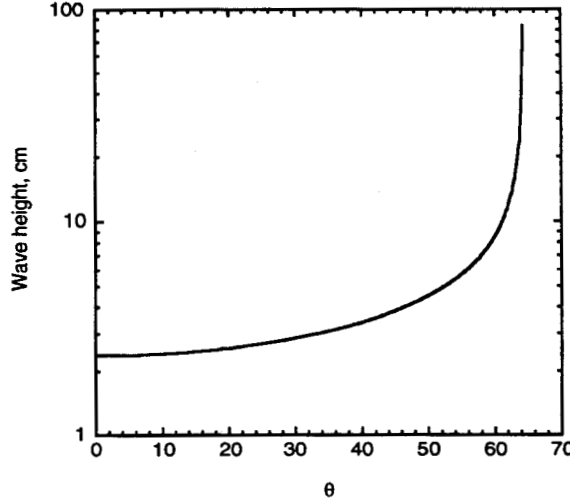


Fig. 15: The scale of the ocean wave heights defining the onset of incoherent scattering based on the Raleigh criterion

There are several important considerations when the reflection is coherent:

(1) When the ocean surface is rough, the reflected signal is scattered in all directions with weights specified by the surface scattering cross section. When the ocean surface is smooth and scattering is coherent, the reflection is governed by geometrical optics where Snell's law is applied locally at each point of the surface. In this case, the radar equation (Eq. (3)) breaks down and the ratio of the scattered to the incident power is given by

$$\frac{P_r}{P_i} = \frac{1}{4} \frac{R^2}{\left(\frac{R \sin \epsilon}{2} + d \right) \left(\frac{R}{2 \sin \epsilon} + d \right)} R_F^2 \quad (16)$$

where R is the Earth's radius, R_F is the Fresnel reflection coefficient and the other variables are defined in Fig. 2. In the limit of small ϵ , the right-hand side of Eq. (16) reduces to $(RR_F^2 \sin \epsilon / 2d)$ which implies that the reflected signal is defocused due to the Earth's curvature. For $\epsilon = 2^\circ$, $d = 700$ km, $R_F^2 \approx 0.6$ for right-hand circularly polarized (RCP) reflected signal, this factor is $\sim 10\%$, which implies that the reflected signal is dominantly RCP and is ~ 10 dB down from the direct signal. Therefore, with a modest antenna gain, the phase of the signal can be tracked by a phase-locked loop with centimeter level accuracy.

(2) The phase measurement can be interpreted as the change of range. This physical meaning is not valid for incoherent reflections, making the phase measurement of no value when it is incoherent, notwithstanding the extreme difficulty in tracking it in this case. The

1 m range measurement error expected with a 20 dB antenna is of interest only after averaging over a very large number of measurements. It takes 10,000 range measurements to average down the random error to 1 cm, which is at the level of accuracy of one phase measurement.

(3) The footprint is no longer set by the P-code chip length but by the carrier wave length (i.e., the first Fresnel zone). The size of the footprint would be given by the dashed and dotted curves of Fig. 6 scaled by a factor of about $\sqrt{12}$ (the square root of the ratio of the P-code chip to the carrier wavelength), therefore smaller than 10-80 km in the incidence plane and 2 km in the normal plane.

These considerations make measurements of coherent reflections invaluable. They also imply that, with proper and fairly simple modifications to the flight receiver, and antenna pointed toward the limb for the purpose of collecting GPS occultations, the system can be used for ocean reflection sensing.

7. Discussion and Conclusion

The fundamental characteristics of bistatic altimetry performed using the GPS signal scattered off the ocean surface and collected by a receiver in space are introduced. The advantages of the dense and rapid surface coverage afforded by the existing GPS and GLONASS transmitters could enable new oceanographic applications such as eddy monitoring and tracking of fast barotropic waves if a constellation of receivers were tracking all the available reflections. To exploit the wealth of potentially available measurements, it is recommended that the pointing direction for the receiving antenna system should be able to move away from the satellite nadir and cover all azimuthal directions. The associated instrument footprint and coherence time are discussed and the implications in terms of receiver design are also outlined.

The theoretical reflected signal is then derived by extension of the cross-correlation process used for direct GPS signals and the characteristics of the leading edge are discussed, to identify analogies and differences with the traditional altimetry waveform. In particular, the derivative of the leading edge exhibits a narrow peak corresponding to the time of arrival of the specular point reflection. This suggests a novel useful algorithm for extracting the mean sea height. This feature, peculiar to the GPS spread-spectrum signal, stems from the cross-correlation operation performed in the receiver and is not shared by the traditional altimeter waveform.

The effects of ionosphere, troposphere and clock errors on the accuracy of the altimetry measurements are estimated, and an overall range accuracy rms value is predicted as a function of sea state and antenna gain. When averaging many measurements collected from a possible constellation of receivers, the range error is progressively reduced as a function of space and time, yielding predicted accuracies in sea height estimation with associated spatial and temporal resolutions. Preliminary calculations indicate that sea height accuracies of a few cm on spatial scales of 100 Km from measurements averaged over four days could be achievable.

The effect of wind speed and significant wave height on the received signal is discussed and simulations are performed for a realistic range of wind speeds and wave heights, respectively. In particular, it is stressed that the bistatic geometry makes the sea height measurements less sensitive to wave heights than the conventional nadir viewing geometry. This results in a reduced EM-bias as well. The range accuracy versus receiving antenna gain and scattering direction is discussed and a specific guideline on the gain necessary for altimetry from space is provided. In particular, at low elevation angles both scattering cross

section and coherence time increase over the nadir case, thus resulting in a potential decrease of the range error for a fixed antenna gain. Finally, considerations on the possibility to track phase at small elevation angles and the resulting improvement in the range measurement accuracy are presented.

Acknowledgments

We thank Larry Romans of JPL for help in producing figure 1. Research described in this paper was performed at the Jet Propulsion Laboratory, California Institute of Technology, under funding from the NASA Office of Earth Science.

References

- 1 – Wu, S.C., L. J. Romans and L. E. Young, "A Novel GPS-Based Sensor for Ocean Altimetry," proceedings of IEEE Int. Geos. & Remote Sensing Symp., Seattle, WA, July, 1998. (George, you have 2 references to Wu in 1997 and 1998)
- 2 – Martin-Neira, M., "A passive reflectometry and interferometry system (PARIS): application to ocean altimetry," ESA Journal, vol. 17, pp. 331-355, 1993.
- 3 – Picardi, G., R. Seu, S. G. Sorge and M. Martin-Neira, "Bistatic model of ocean scattering," IEEE Transactions on antennas and propagation, Vol. 46, n. 10, pp. 1531-1541, Oct. 98.
- 4 – Garrison, J.L., S.J. Katzberg and M.I. Hill, "Effect of sea roughness on bistatically scattered range coded signals from the Global Positioning System," Geophys. Res. Lett., 25, 2257-2260, 1998.
- 5 – Lin, B., S.J. Katzberg, J.L. Garrison and B.A. Wielicki, "Relationship between GPS signals reflected from sea surfaces and surface winds: Modeling results and comparisons with aircraft measurements," J. Geophys. Res., Vol. 104, n. C9, pp. 20,713-20,727, Sept. 1999.
- 6 – Zavorotny, V.U. and A. G. Voronovich, "Scattering of GPS signals from the ocean with wind remote sensing application," accepted for publication in IEEE Transactions on Geoscience and Remote Sensing, 1999.
- 7 – Lowe, S.T, J.L. Labrecque, C. Zuffada, L.L. Romans, L.E. Young and G.A. Hajj, "First spaceborne observation of an Earth-reflected GPS signal", submitted for publication in Journal of Geophysical Research, 1999.
- 8 – Brown, G. S., "Backscattering from a gaussian-distributed, perfectly conducting rough surface," IEEE Transactions on antennas and propagation, vol. 26, pp. 472-482, 1978.
- 9 – Elfouhaily, T., B. Chapron, K. Katsaros and D. Vandemark, "A unified directional spectrum for long and short wind-driven waves," J. Geophys. Res., vol. 102, pp. 15,781-15,796, 1997.
- 10 – Komjathy, A., V. U. Zavorotny, P. Axelrad, G. Born and J. Garrison, "GPS signal scattering from sea-surface: comparison between experimental data and theoretical model," Proceedings of the 5th Int. Conference on remote sensing for marine and coastal environments, vol. 1, pp. 530-539, Oct. 98.
- 11 – Brown, G. S., "The average impulse response of a rough surface and its applications" IEEE Transactions on antennas and propagation, vol. 25, n. 1, pp. 67-74, Jan 1977.
- 12 – Barrick, D.E. and B. J. Lipa, "Analysis and interpretation of altimeter sea echo," in Satellite oceanic remote sensing, Adv. in geophys., vol. 27., ed B. Saltzman, pp. 61-100, 1985.
- 13 – Srokosz, M.A., on the joint distribution of surface elevation and slopes for a nonlinear random sea, with applications to radar altimetry, J. Geophys. Res., vol. 91, n. C1, pp. 995-1006, 1986.
- 14 – Rodriguez, E., "Altimetry for non-gaussian oceans: height biases and estimation parameters," J. Geophys. Res., vol. 93, n. C11, pp. 14,107-14,120, Nov. 1988.

- 15 - Thomas, J. B., "Signal-processing theory for the turborogue receiver," JPL publication 95-6, April 1995.
- 16 - Fung, A.K, C. Zuffada and C.Y. Hsieh, "Incoherent bistatic scattering from the sea surface at L-band, submitted for publication in IEEE Transactions on Geoscience and Remote Sensing, 1999.